

A few extreme events dominate global interannual variability in gross primary production

This content has been downloaded from IOPscience. Please scroll down to see the full text.

View [the table of contents for this issue](#), or go to the [journal homepage](#) for more

Download details:

This content was downloaded by: jzsch

IP Address: 141.5.17.110

This content was downloaded on 05/03/2014 at 17:16

Please note that [terms and conditions apply](#).

# A few extreme events dominate global interannual variability in gross primary production

Jakob Zscheischler<sup>1,2,3</sup>, Miguel D Mahecha<sup>1</sup>, Jannis von Buttlar<sup>1</sup>, Stefan Harmeling<sup>2</sup>, Martin Jung<sup>1</sup>, Anja Rammig<sup>4</sup>, James T Randerson<sup>5</sup>, Bernhard Schölkopf<sup>2</sup>, Sonia I Seneviratne<sup>3</sup>, Enrico Tomelleri<sup>1,6</sup>, Sönke Zaehle<sup>1</sup> and Markus Reichstein<sup>1</sup>

<sup>1</sup> Max Planck Institute for Biogeochemistry, Hans-Knöll-Straße 10, D-07745 Jena, Germany

<sup>2</sup> Max Planck Institute for Intelligent Systems, Spemannstraße 38, D-72076 Tübingen, Germany

<sup>3</sup> Institute for Atmospheric and Climate Science, Universitaetstrasse 16, ETH Zürich, 8092, Switzerland

<sup>4</sup> Potsdam Institute for Climate Impact Research, Telegrafenberg 31, D-14473 Potsdam, Germany

<sup>5</sup> Department of Earth System Science, Croul Hall, University of California, Irvine, CA 92697, USA

<sup>6</sup> EURAC, Institute for Applied Remote Sensing, Drususallee 1, I-39100 Bozen, Italy

E-mail: [jzsch@bgc-jena.mpg.de](mailto:jzsch@bgc-jena.mpg.de)

Received 8 January 2014, revised 4 November 2013

Accepted for publication 17 January 2014

Published 4 March 2014

## Abstract

Understanding the impacts of climate extremes on the carbon cycle is important for quantifying the carbon-cycle climate feedback and highly relevant to climate change assessments. Climate extremes and fires can have severe regional effects, but a spatially explicit global impact assessment is still lacking. Here, we directly quantify spatiotemporal contiguous extreme anomalies in four global data sets of gross primary production (GPP) over the last 30 years. We find that positive and negative GPP extremes occurring on 7% of the spatiotemporal domain explain 78% of the global interannual variation in GPP and a significant fraction of variation in the net carbon flux. The largest thousand negative GPP extremes during 1982–2011 (4.3% of the data) account for a decrease in photosynthetic carbon uptake of about 3.5 Pg C yr<sup>-1</sup>, with most events being attributable to water scarcity. The results imply that it is essential to understand the nature and causes of extremes to understand current and future GPP variability.

Keywords: spatiotemporal extreme events, GPP, power law

## 1. Introduction

Climate extremes such as droughts, heat waves or intense precipitation events are increasingly perceived as key players in the Earth system and are expected to increase in the wake of climate change (IPCC 2012, Barriopedro *et al* 2011, Sillmann *et al* 2013). The associated impacts on terrestrial ecosystems

are diverse and difficult to determine (Smith 2011, Ma *et al* 2012, Reichstein *et al* 2013). Some of these aspects are directly observable, for instance via crop damage (Piao *et al* 2010), and thus related to food scarcity (Rosenzweig *et al* 2001), or forest destruction by windthrow or fire (Chen *et al* 2011). Several studies have shown, however, that climate extremes can influence the terrestrial biosphere in less easily detectable ways, for instance by altering the carbon budget via a reduction of primary productivity (Piao *et al* 2010, Barriopedro *et al* 2011, Lewis *et al* 2011, Ma *et al* 2012). This aspect is crucial for an assessment and attribution of extreme anomalies in the



Content from this work may be used under the terms of the [Creative Commons Attribution 3.0 licence](https://creativecommons.org/licenses/by/3.0/). Any further distribution of this work must maintain attribution to the author(s) and the title of the work, journal citation and DOI.

carbon cycle. Hence, in this study, we aim to provide a global quantification of extreme anomalies in the photosynthetic carbon uptake, understand its implications for the carbon balance and attribute large-scale negative extremes to climatic drivers or fires.

In contrast to earlier studies which analyzed climate extremes and their effects on the carbon cycle (Potter *et al* 2003, Ciais *et al* 2005, Reichstein *et al* 2007, Zhao and Running 2010, Barriopedro *et al* 2011, Lewis *et al* 2011, Ma *et al* 2012), our work is based on two major innovations. First, we adopt an ‘impact perspective’ (Smith 2011, Reichstein *et al* 2013) by directly evaluating extreme changes within the biosphere. In particular, we analyze four different data products of gross primary production (GPP) covering the last 30 years, two data-driven GPP estimates and two global carbon-cycle models. On the data-driven side we use the upscaled eddy-covariance-based GPP estimates (MTE, Jung *et al* 2011) and the light-use efficiency based MOD17+ (Running *et al* 2004). The models we use include a process-based global ecosystem model (Lund–Potsdam–Jena Dynamic Global Vegetation Model for Managed Land, LPJmL, Sitch *et al* 2003), and a land-surface model (OCN, Zaehle and Friend 2010). Second, we perform a complete three-dimensional (spatiotemporal) assessment of extremes based on a recently developed methodology (Lloyd-Hughes 2012, Zscheischler *et al* 2013). Aiming for irregularities of global relevance we identify extreme events that are contiguous in both space and time (three-dimensional events in the data cube, figure A.1). Adapted from Zscheischler *et al* (2013), we compute extremes using a range of percentiles (upper and lower 1 to 10% of the anomalies, figure A.2, Seneviratne *et al* 2012). Our analysis then focuses on the largest extreme events where the impact of an event is determined by the GPP anomalies integrated over the spatiotemporal extent of the event. To estimate the impact of GPP extremes on the terrestrial net carbon balance we rely on net ecosystem exchange (NEE) estimates from Carbon-Tracker (Peters *et al* 2007) and estimates for the residual land sink (RLS, defined as the atmospheric increase in CO<sub>2</sub> minus emissions from fossil fuels minus net emissions from changes in land use minus oceanic uptake (Le Quéré *et al* 2013)).

## 2. Materials and methods

The core ingredients of this paper are two recently developed tools to first identify large-scale extreme events in variables characterizing the state of the biosphere and second attribute them to climatic drivers (Lloyd-Hughes 2012, Zscheischler *et al* 2013). The new element in the identification step is to combine individual extremes to three-dimensional extreme events to provide a robust assessment of large-scale extremes even when data sets contain uncertainties. In the attribution step we essentially test whether environmental conditions during a particular extreme event in GPP were extremely different compared to all other times in the available time period. After introducing the different data sets, in this section we explain in detail how we use these two approaches on our data sets.

### 2.1. Data

To identify extreme events that are relevant to the terrestrial biosphere, we rely on four different data sets describing gross primary production (GPP; all used datasets with their abbreviations are listed in table A.1).

MTE (Jung *et al* 2011) involves training a model tree ensemble at site level using FLUXNET (a global network of eddy-covariance observations in tandem with site level meteorology, Baldocchi *et al* 2001) to extrapolate to large spatiotemporal domains. We use a fully data-driven upscaling product that relies mainly on a composite of different remote sensing fAPAR products but also uses climate data from ERA interim. (fAPAR is the fraction of absorbed photosynthetically active radiation, a satellite remote sensing proxy for photosynthetic activity.)

MOD17+ (Running *et al* 2004) is derived using the same model structure as the MODIS GPP data stream (Running *et al* 2000) linking shortwave incoming radiation, minimum temperature and vapor pressure deficit. The parameterization of the MOD17+ model follows Beer *et al* (2010); i.e., it is based on Bayesian inversion against GPP time series from FLUXNET. The model parameters are calibrated against GPP time series from the FLUXNET measurement network through a Bayesian data model synthesis. The terms in the MODIS-MOD17 biome-specific look-up table are used as priors. For regionalizing the model parameters we stratify the results of the *in situ* calibration per vegetation type and bioclimatic class. As climatic drivers we use the ERA-interim dataset and the same composite of fAPAR products as in MTE (Jung *et al* 2011).

LPJmL (Sitch *et al* 2003) is a dynamic global vegetation model (DGVM) with a fully coupled carbon and water cycle. Vegetation productivity, i.e. GPP, is derived by a process-based photosynthesis scheme that adjusts carboxylation capacity and leaf nitrogen seasonally and within the canopy profile. For the present study, LPJmL is run in its natural vegetation mode driven by ERA-interim temperature, radiation and precipitation.

OCN (Zaehle and Friend 2010) is a land-surface model derived from the ORCHIDEE DGVM (Krinner *et al* 2005), which prognostically simulates foliar area and N content and employs a two-stream radiation scheme coupled to the process-based calculation of photosynthesis in light-limited and light-saturated chloroplasts within each canopy layer.

To attribute negative extreme events in GPP to (extreme) climatic drivers and fire events we use temperature ( $T$ ) and precipitation ( $P$ ) from ERA-Interim (Dee *et al* 2011), burned area (BA) and CO<sub>2</sub> emissions from fires (FE, Giglio *et al* 2010), and the water availability index (WAI). WAI is a surrogate for soil moisture and was computed using daily precipitation and potential evapotranspiration data from bias-corrected ERA interim and a map of plant available water holding capacity from the Global Harmonized World Soil Database (FAO/IIASA/ISRIC/ISSCAS/JRC 2012). Using WAI or variants of it as a proxy for soil moisture has a long tradition in ecosystem modeling (Federer 1982, Aber and Federer 1992, Prentice *et al* 1993, Kleidon and Heimann 1998). The parameter used in the calculation of the WAI was

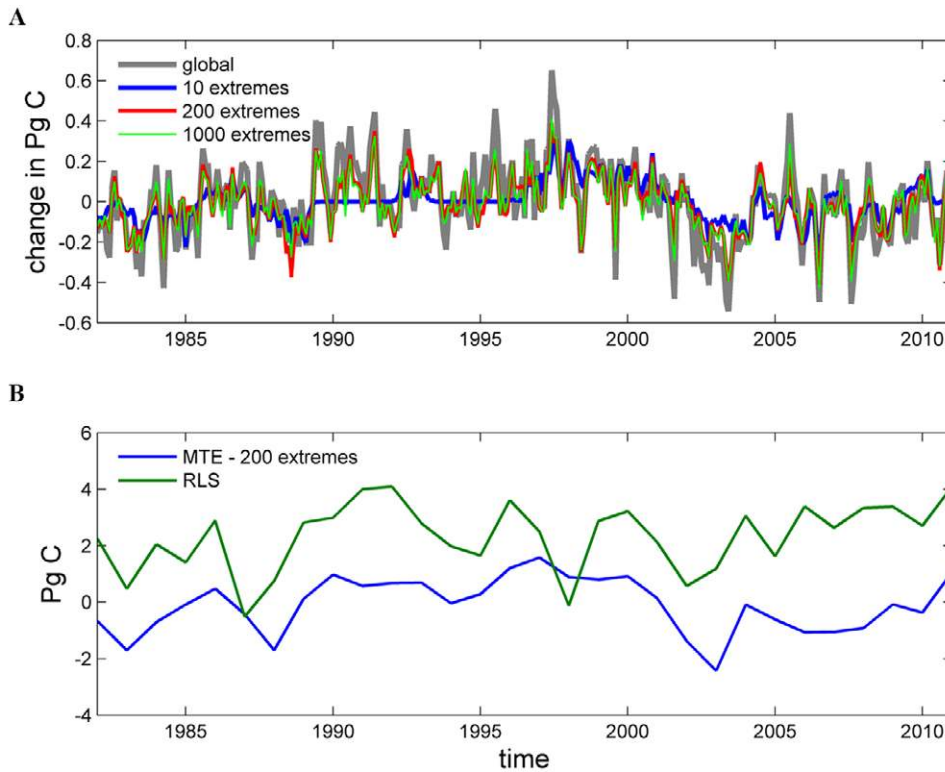


**Figure 1.** Extremes in MTE GPP in relation to global GPP anomaly and the global land carbon sink. (A) Global GPP anomaly (gray); 10, 200, and 1000 largest positive and negative tenth-percentile extremes in GPP (blue, red, and green lines, respectively), monthly time scale. All pixels which are extreme at a certain time step are summed together to obtain one value for each time step. (B) Residual land sink (Le Quéré *et al* 2013) (green) and 200 largest GPP extremes using the tenth-percentile definition (blue).

taken as the median value of 15 sites from the synthesis study of *in situ* data by Teuling *et al* (2006). We use low values of water availability as an index for drought.

The spatial resolution for all the above data sets is 0.5°. *T*, *P*, WAI and all GPP data sets are available monthly from 1982 to 2011, BA and FE from 1997 to 2010. Table A.1 gives a summary of all used data sets of this gridded format.

To relate extremes in GPP to net ecosystem exchange (NEE) we downloaded monthly data from CarbonTracker for the years 2000–2011 (CT2011\_oi, <http://carbontracker.noaa.gov>, Peters *et al* 2007) and aggregated them to global anomalies. To obtain the residual land sink (RLS) we rely on the Global Carbon Project (GCP, [www.globalcarbonproject.org](http://www.globalcarbonproject.org)) and use yearly data from 1982–2011 (Le Quéré *et al* 2013).

**2.2. Preprocessing**

We follow the suggestions from Zscheischler *et al* (2013). In particular, for *T*, WAI and all GPP data sets we first subtract the linear trend and mean annual cycle per grid cell. We divide the less smooth variables *P*, BA and FE at each pixel by the sum of the respective time series at that grid cell. We call the resulting values after preprocessing *anomalies*. The goal of the preprocessing is to obtain time series which depict deviations from the mean behavior.

**2.3. Extreme event identification**

In accordance with the IPCC climate extreme classifications (Seneviratne *et al* 2012), we define *extremes* as the occurrence of certain values in the tails of the probability distribution

of the anomalies. We adapt the methodology described in Zscheischler *et al* (2013) and define extremes to be outside a certain threshold *q*, which is defined by a percentile on the absolute values of the anomalies (figure A.2). We choose the thresholds for each of the four data sets such that extremes (positive and negative together) comprise 1%, . . . , 10% of the anomalies, respectively. We then define an *extreme event* by spatiotemporally contiguous points whose values are larger than *q* (positive extremes) and smaller than  $-q$  (negative extremes), respectively. The size of an extreme event is defined by the integral of the corresponding anomalies of GPP over time and space, i.e. its unit is grams of carbon. Hence, ‘large’ events are determined by their integrated impact of GPP anomalies over their spatiotemporal domain.

To compute correlations with monthly time series of other data sets or map hot spots of extreme events we aggregate extreme events of each GPP dataset individually either in space or in time. For an aggregation in space, at each time step all anomalies which happen to be part of some extreme event (according to the definition under consideration) are summed together (see, e.g., figure 1), yielding one time series of the overall impact of the respective extreme events. This time series of GPP extreme events can then be correlated with e.g. the global GPP or NEE anomaly in order to obtain the fraction of explained variance. Similarly, for an aggregation in time, at a specific location (pixel), all anomalies which happen to be part of some extreme event are summed together (see, e.g., figure 3), yielding a global map of the cumulative impact of the extreme events under consideration.

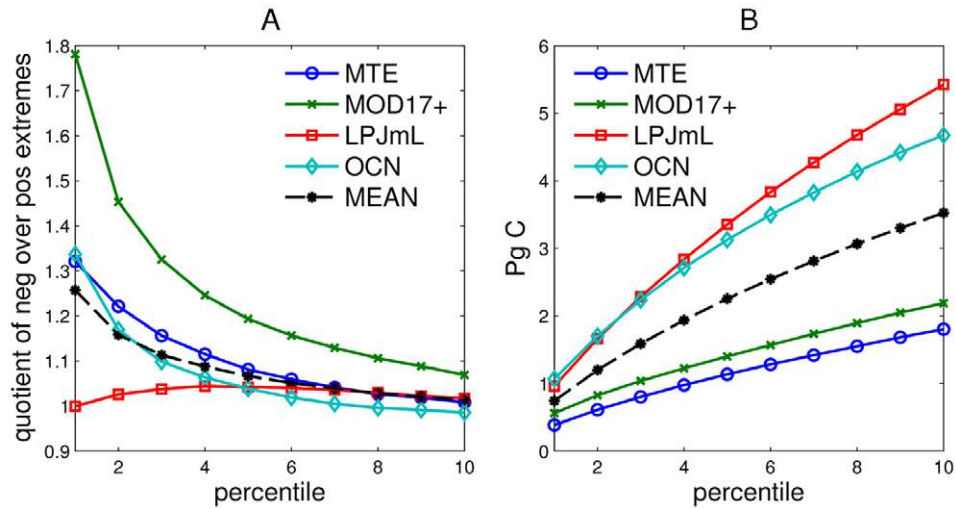


**Figure 2.** Asymmetry between positive and negative GPP extremes and global decrease in gross land carbon uptake due to GPP extremes. Shown are the four data sets MTE (blue circles), MOD17+ (green crosses), LPJmL (red squares), and OCN (cyan diamonds) and their mean (black dashed stars). (A) Quotient of accumulated changes in gross land carbon uptake due to the 1000 largest negative events over the 1000 largest positive events for different percentiles (1%–10%). (B) Global accumulated decrease in GPP due to the 1000 largest negative GPP extremes as a function of the percentile definition. Shown are the accumulated decreases in petagrams of carbon per year ( $10^{15}$  g C yr<sup>-1</sup>).

We further define the *asymmetry* between negative and positive GPP extremes as the quotient of the size of  $n$  negative events over  $n$  positive events. Throughout the text, we usually report the fraction exceeding unity in percent.

#### 2.4. Attributing drivers to GPP extremes

We intend to identify drivers that possibly caused negative extreme events in GPP. To this end, for a certain negative GPP extreme event we compute the median of a driver variable over the spatiotemporal domain of the event. By shifting the event in time and computing such medians for each possible time step, we obtain a test statistic for each driver variable and each GPP extreme (see also Zscheischler *et al* 2013). We then compute  $p$ -values for the 100 largest GPP extreme events using the first-percentile definition by considering the drivers  $T$ ,  $P$ , WAI, BA, and FE. For  $T$  and  $P$  we take both right- and left-sided  $p$ -values into account (heat waves and cold spells, excessive and exceptionally low precipitation). For WAI we consider only the left-sided  $p$ -value (water scarcity), for BA and FE only the right-sided  $p$ -value (fire events). We count a driver as a cause if its  $p$ -value is smaller than 0.1 (see table A.5 for a summary of significant drivers). Other thresholds are possible but do not affect the conclusions of this study. If a driver's  $p$ -value is below 0.1 one or several months before the GPP extreme event, we assume that the GPP extreme is a lagged response to the extreme driver. In this study we take time lags of a maximum of three months into account.

### 3. Results

#### 3.1. A few extremes explain most of the global interannual variability

The size distribution of extreme events can often be well approximated by a power law relationship  $f(x) \sim x^{-\alpha}$ , where  $x$  is the size of an extreme event and  $\alpha$  is the so-called scaling

exponent (Ghil *et al* 2011). It has been recently shown that extremes in fAPAR can be likewise approximated well by a power law (Zscheischler *et al* 2013, Reichstein *et al* 2013). We also find power laws for the size distribution of extremes in GPP (here, the size of an extreme is its impact on GPP, figure A.3). The scaling exponent  $\alpha$  is below 2 for most data sets and percentiles, indicating that a few exceptionally large extremes dominate the whole distribution of extremes (Fisher *et al* 2008).

Assuming that local extreme events in GPP can be of global relevance, the discovered power law behavior suggests that only a few events cause globally relevant impacts. To investigate this hypothesis, we correlate time series of integrated GPP extremes with the global GPP anomaly. We find that 78% ( $\pm 5$ ) of the global GPP anomaly can be explained by the largest 200 tenth-percentile GPP extreme events (positive and negative, figure 1(A) for the case of MTE; figure A.4(A) for all data sets). These extreme events occur on only 7% ( $\pm 0.6$ ) of the spatiotemporal domain (figure A.4(B)), revealing the strong spatial heterogeneity inherited from the power law distribution. By choosing a subset of the largest events we at the same time focus on the more robust features of the data sets.

The question is, however, how the identified extremes in GPP translate into anomalies of the land carbon balance. We find that same extreme events (the 200 largest tenth-percentile extreme events in GPP) explain 8.4% ( $\pm 0.03$ ,  $p < 0.001$ ) of the variability in monthly anomalies of global NEE over the years 2000–2011. In addition, in the case of MTE, the same extreme events explain 22% of the annual variability in RLS for the entire time period ( $p < 0.01$ , figure 1(B)). MTE is the data set closest to actual observations (it uses site level CO<sub>2</sub> flux observations compiled in FLUXNET in tandem with satellite derived data of fAPAR), which might explain its prominent role in yielding significant correlations with RLS. Very strong correlations between extremes in GPP and variability in NEE, or even the atmospheric CO<sub>2</sub> growth

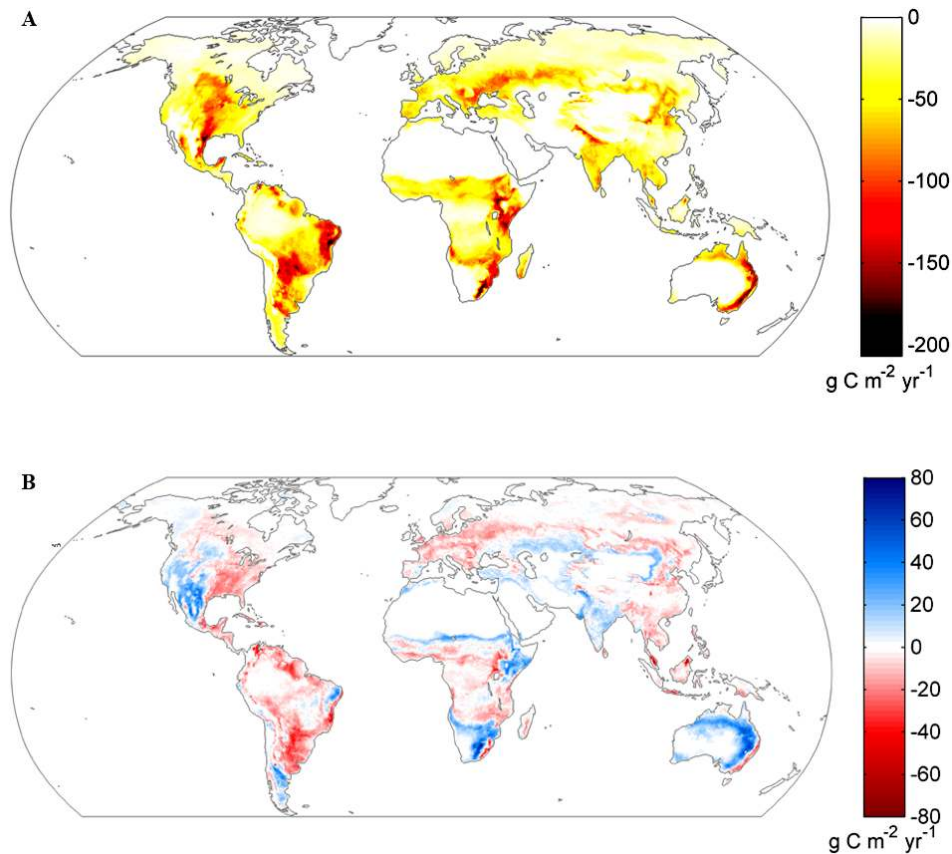


**Figure 3.** Global distribution of GPP extremes. Extremes were computed using the tenth percentile and then averaged over the four GPP data sets (MTE, MOD17+, LPJmL, and OCN) and the time period 1982–2011. Shown are the numbers for an averaged year in grams of carbon per square meter per year ( $\text{g C m}^{-2} \text{yr}^{-1}$ ). (A) Decrease in terrestrial gross land carbon uptake during the 1000 largest negative GPP extremes. (B) Change in gross land carbon uptake due to the 1000 largest positive and negative GPP extremes.

rate, cannot be generally expected because of the strong, but complex and regionally varying, coupling of GPP and ecosystem respiration (Richardson *et al* 2007, Mahecha *et al* 2010). Lagged and legacy effects of climate extremes which can significantly alter various components of the terrestrial carbon cycle additionally mask the immediate translation of GPP extremes on NEE (Reichstein *et al* 2013).

### 3.2. Negative extremes are larger than positive extremes

The decrease of GPP associated with negative extremes is globally only partly compensated by positive GPP extremes. Negative GPP extreme events are on average up to 25% larger compared to positive extreme events if we consider the 1000 largest events on both tails of the distribution (figure 2(A)). While the data spread is large (ranging from 0% in LPJmL to 80% in MOD17+ for the first-percentile definition, figure 2(A), tables A.2 and A.3), all models show an asymmetry towards more decrease in gross land carbon uptake (negative extremes) for nearly all used percentiles. Moreover, this asymmetry is stronger if one considers fewer of the largest events and more extreme percentiles (figures 2(A) and A.5). According to the ‘slow in, rapid out’ principle for net ecosystem exchange (Körner 2003), the observed asymmetry might originate in e.g. a few large disturbance events such as droughts, fires or insect outbreaks that lead

to often an instantaneous decrease in carbon uptake (negative GPP extremes). Excess productivity (positive GPP extremes, e.g. due to regrowth), in contrast takes place on much longer timescales (Bengtsson *et al* 2003, Dore *et al* 2008). The observed asymmetry could also be originated in asymmetric driving mechanisms (e.g. climate extremes). Skewed distributions in drivers due to amplifying feedbacks such as those between droughts and heat waves (Mueller and Seneviratne 2012) might cause disproportionately large decreases in carbon uptake.

We will focus on negative GPP extremes for most of the remainder. The cumulative effect of negative extremes depends strongly on the percentile used. Averaged over the four GPP data sets, the 1000 largest negative extremes based on the first-percentile definition yield a decrease in gross land carbon uptake of about  $0.7 \text{ Pg C yr}^{-1}$ , in contrast to  $2.2 \text{ Pg C yr}^{-1}$  on the fifth- and  $3.5 \text{ Pg C yr}^{-1}$  on the tenth-percentile definition (figure 2(B); for comparison, yearly photosynthetic carbon uptake ranges between 110 and  $160 \text{ Pg}$  in our data sets). Both the estimates for the two data-driven approaches as well as the estimates from the terrestrial biosphere models agree well among each other. However, the estimates of the models exceed the data-based estimates by a factor of more than two (figure 2(B), table A.2). The difference in the size of the extremes between these two sets is mainly due to different magnitudes in the anomalies (table A.4) but the timing of extremes is highly correlated

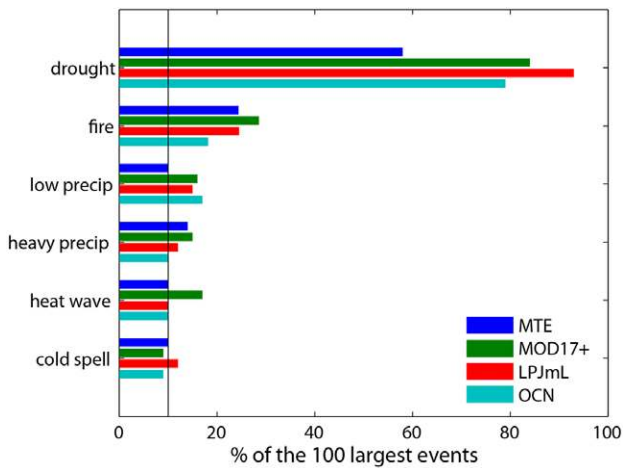


**Figure 4.** Attribution of negative extremes in GPP to climate drivers and fire. Shown are percentages of 1%-extreme events in GPP out of the largest 100 that could be associated with extreme drivers (methodology adapted from Zscheischler *et al* 2013). For fire not all 100 fall into the range where fire data is available (table A.5). We chose *p*-values below 0.1 as being extremes for the drivers and considered a maximal time lag of 3 months. Thus, the horizontal line at 10% depicts the percentage of associations expected if the data sets were random. How labels at the y-axis are defined can be found in table A.5.

(figure A.6). It has been shown before that some models tend to overestimate interannual variability (Keenan *et al* 2012), while data-driven approaches rather underestimate interannual variability (Jung *et al* 2011). We hence assume that data-driven and process-driven estimates of GPP describe a reasonable envelope for the real size of the extremes.

The geographical hotspots of negative GPP extremes are found in Northeastern Brazil (matching with earlier observations, Potter *et al* 2003), Central South America, Southeastern Australia, South Africa, Kenya, Tanzania and South Central United States (up to more than 180 g C m<sup>-2</sup> yr<sup>-1</sup> decrease in GPP, figure 3(A)). In regions of Eurasia and North America the absolute decrease in GPP during extreme events is smaller (up to 100 g C m<sup>-2</sup> yr<sup>-1</sup>) because the average GPP is lower. The individual patterns for the four data sets broadly agree with each other, although there are significant differences at a regional scale (figure A.7). MOD17+ is the only data set showing extremes in the Amazon. MTE shows a hot spot in Eastern China, which is not seen by the other data sets (figure A.7). Overall, the hot spots agree well with negative extreme events on remotely sensed variables describing the state of the biosphere such as fAPAR (figure 6 in Zscheischler *et al* 2013) and the enhanced vegetation index (EVI, figure A.8, obtained with the same methodology). To address the relative changes in gross land carbon uptake due to negative GPP extremes, we divide the globe into the 26 IPCC regions (IPCC 2012) (figure A.9). Northern Australia (region 25) on average experiences the largest relative decrease in gross land carbon uptake (nearly 7%) followed by the Central United States (region 8) with around 5.5% decrease (figure A.10). While we find most positive and negative GPP extremes in similar areas, particularly in Europe and in tropical areas negative GPP extremes are dominating (figure 3(B)).

### 3.3. Most negative extremes are driven by water scarcity

Various environmental drivers can lead to extreme reductions in GPP (Reichstein *et al* 2013). We investigate extreme temperatures, extreme precipitation, droughts or fires as possible drivers using recently developed tools (Zscheischler *et al* 2013) and find that negative GPP extremes are most often associated with anomalous low values of water availability (between 58 (MTE) and 93 (MOD17+) events out of the 100 largest, figure 4). Associations with extreme temperature and precipitation are not found that often. GPP in MOD17+ is most susceptible to fire: 18 out of the 63 negative GPP extremes that fall in the range where fire data is available (29%) can be associated with fire (figure 4, table A.5). Differences in the number of events associated with a certain driver reflect varying climate sensitivity between the four data sets. Overall, we associate in each data set more than 70 of the 100 largest negative GPP extremes to extreme temperatures or precipitation, low water availability, or fires (table A.5, last column). In line with regional studies (Zhao and Running 2010, Ciais *et al* 2005, Ma *et al* 2012), we conclude that on a global scale, water deficit is the main driver for negative GPP extremes (figure 4). High temperature extremes and heavy precipitation events play a subordinate role at the global scale although they may be of regional relevance. The data products and models used, however, may also underestimate the effects of e.g. extreme high temperatures on vegetation activity and legacy effects. Other causes for extreme anomalies in GPP might be large disturbances such as pest outbreaks, extreme winds, and human deforestation.

## 4. Conclusions

Understanding the behavior and characteristics of extreme events in climate and carbon fluxes are important for the projections of the current land carbon sink (Reichstein *et al* 2013) and future vulnerability assessments (IPCC 2012). Directly studying extreme responses in the biosphere opens innovative possibilities for research within the disturbance and carbon-cycle science communities. Our study reveals that a few extreme events in GPP events explain most of its interannual variability and contribute a small but significant amount to the variability in the net carbon balance, although they occur on only a small fraction of the land surface. These results imply that to understand current and future GPP variability it is essential to understand the nature and causes of extremes. Our results also highlight the importance of hydrometeorological extremes for carbon-cycle variability at the global scale. Thus, expected alterations of the water cycle in future (Sillmann *et al* 2013, Huntington 2006) will likely have a large effect on carbon-cycle extremes and global interannual variability.

## Acknowledgments

This work was funded by the European Commission projects CARBO-Extreme (FP7-ENV-2008-1-226701) and GEOCARBON (FP7-ENV-2011-283080). We thank W von Bloh for setting up the LPJmL model code. JZ and JvB are part of the International Max Planck Research School for Global Biogeochemical Cycles (IMPRS-gBGC).

Appendix

**Table A.1.** Datasets of drivers (left) and responses (right) with reference.

Driver variables used for attribution		Response/impact variables	
<i>T</i> (Dee et al 2011)	Temperature (ERA interim)	MTE (Jung et al 2011)	GPP, model tree ensemble
<i>P</i> (Dee et al 2011)	Precipitation (ERA interim)	MOD17+ (Beer et al 2010, Running et al 2004)	GPP, light-use efficiency model
WAI (Prentice et al 1993)	Water availability index	LPJmL (Sitch et al 2003)	GPP, global ecosystem model
BA (Giglio et al 2010)	Burned area	OCN (Zaehle et al 2010, Zaehle and Friend 2010)	GPP, land-surface model
FE (Giglio et al 2010)	CO <sub>2</sub> fire emissions	EVI (Huete et al 2002)	Enhanced vegetation index

**Table A.2.** Overall sums of the integrals of the largest 1000 extremes in GPP for the four data sets MTE, MOD17+, LPJmL, and OCN from January 1982 to December 2011 in petagrams of carbon per year (10<sup>15</sup> g C yr<sup>-1</sup>). Shown are both negative and positive extremes using the first-, fifth- and tenth-percentile definitions. For comparison, the last column displays the averaged uptake of the terrestrial biosphere per year.

	1%	5%	10%	90%	95%	99%	Total
MTE	0.39	1.14	1.80	1.79	1.05	0.29	121
MOD17+	0.56	1.40	2.19	2.05	1.17	0.32	104
LPJmL	0.96	3.35	5.42	5.33	3.22	0.96	161
OCN	1.07	3.13	6.68	6.74	3.01	0.80	136

**Table A.3.** Difference between positive and negative extremes in units of petagrams of carbon per year (Pg C yr<sup>-1</sup>). Shown is the difference between overall sums of integrals of the largest 1000 extremes in GPP for the four data sets MTE, MOD17+, LPJmL, and OCN from January 1982 to December 2011 for extremes using the first-, fifth- and tenth-percentile definitions.

	1%: pos-neg	5%: pos-neg	10%: pos-neg
MTE	-0.09	-0.08	-0.01
MOD17+	-0.25	-0.27	-0.14
LPJmL	0	-0.13	-0.09
OCN	-0.27	-0.12	0.07

**Table A.4.** Five characteristic variables determining the size of GPP extremes. Shown are the values for the largest negative first- and tenth-percentile extreme events for each of the data sets MTE, MOD17+, LPJmL, and OCN, respectively.

	Size (Pg C)		Spatial extent (10 <sup>6</sup> km <sup>2</sup> )		Mean duration (months)		Mean anomaly (g C m <sup>-2</sup> month <sup>-1</sup> )		Max anomaly (g C m <sup>-2</sup> month <sup>-1</sup> )	
	1%	10%	1%	10%	1%	10%	1%	10%	1%	10%
MTE	-0.3	-1.6	3.1	6.8	1	7	-66	-32	-150	-167
MOD17+	-0.4	-7.4	2.6	14.6	2	14	-79	-37	-180	-225
LPJmL	-0.7	-9.2	2.3	10.5	2	10	-165	-85	-273	-232
OCN	-1.3	-22.5	3.5	9.2	3	33	-133	-75	-215	-260

**Table A.5.** Number of 1%-extreme events in GPP out of the largest 100 that could be associated with extreme drivers (methodology adapted from Zscheischler et al (2013)). Numbers are counts of events with extreme *p*-values (smaller than 0.1) for the four data sets MTE, MOD17+, LPJmL, and OCN with a maximal time lag of 3 months. The numbers in brackets in the second last column indicate the number of events that fall in the time period where fire data were available. The last column sums up all events which have not appeared in one of the former columns.

	$p_r^T < 0.1$ heat wave	$P_l^T < 0.1$ cold spell	$p_r^P < 0.1$ heavy prec	$P_l^P < 0.1$ low prec	$P_l^{WAI} < 0.1$ drought	$p_r^{BA/FE} < 0.1$ fire	Rest
MTE	10	10	14	10	58	10(41)	29
MOD17+	17	9	15	16	84	18(63)	9
LPJmL	10	12	12	15	93	12(49)	6
OCN	10	9	10	17	79	10(55)	14



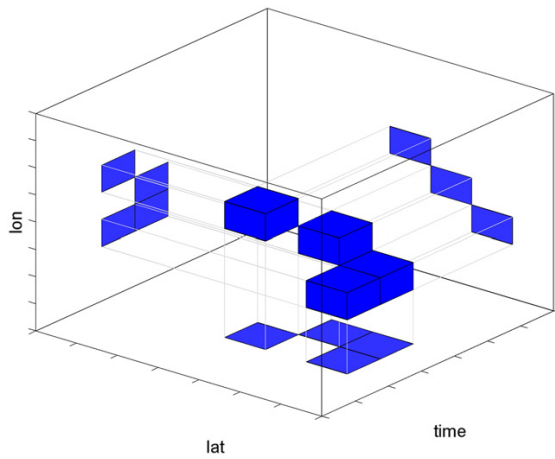


**Figure A.1.** Visualization of four elements in a three-dimensional data cube. In our definition of connectivity these four elements are connected and could form an extreme event. Elements are connected if they have at least one common corner. In other words, in a  $3 \times 3 \times 3$  data cube the element in the center is connected to all other elements in the cube (26).

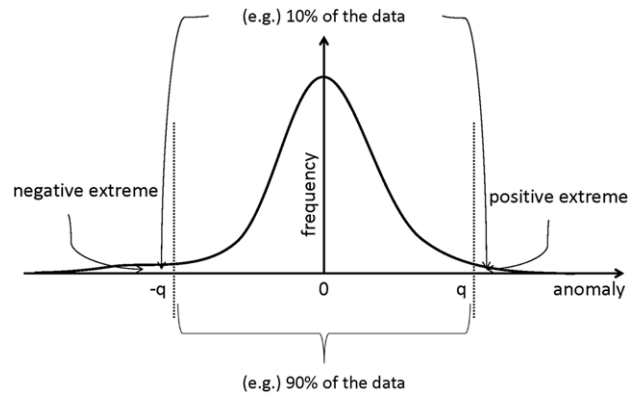


**Figure A.2.** Sketch of how extremes are defined on GPP anomalies. A symmetric threshold  $q$  is set such that (e.g.) 90% of the data anomalies fall in between  $-q$  and  $q$ . Those values which exceed the threshold are defined to be extreme. In this example the extremes are defined using the tenth-percentile definition (not to scale).

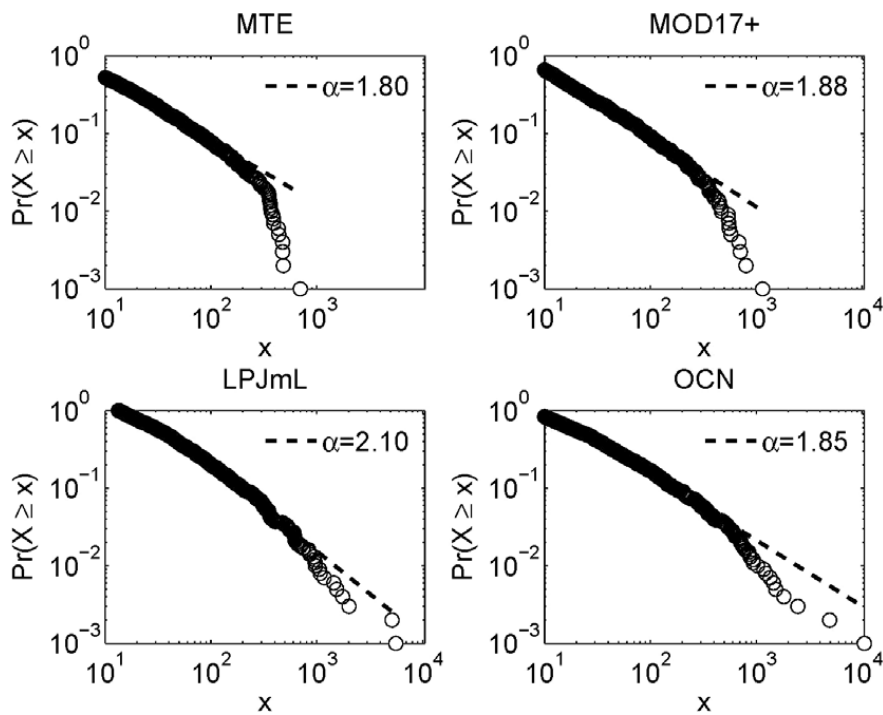


**Figure A.3.** Fitted power law distributions to size of negative GPP extremes for the data sets MTE, MOD17+, LPJmL, and OCN. The power law distribution is given by  $p(x) \sim x^{-\alpha}$ , where  $x$  is the size of an extreme event (in Tg C). Shown is the size distribution for the 1000 largest extreme using the fifth-percentile definition. Every circle is one event, the dashed lines show the exact power law with the respective values of  $\alpha$ . The picture looks similar for positive GPP extremes and other percentiles. Power laws were fitted using the code of Clauset *et al* (2009).

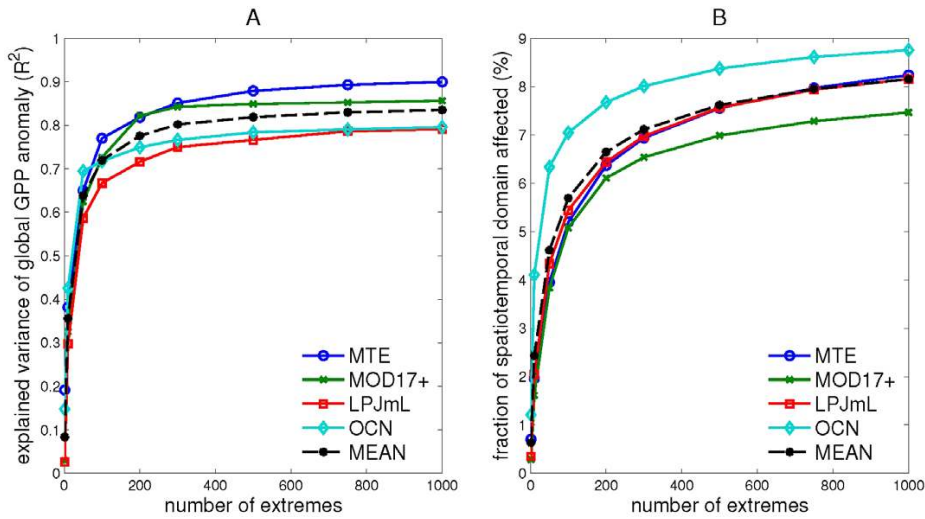


**Figure A.4.** GPP extremes in relation to global interannual variability of GPP. (A) Fraction of explained variance of global anomalies by aggregated positive and negative GPP extremes (tenth-percentile definition). For each time step anomalies and extremes were summed over the whole globe. (B) Percentage of volume of the total spatiotemporal domain (excluding oceans, the Sahara, and Antarctica and Greenland) affected by positive and negative tenth-percentile extremes in GPP.

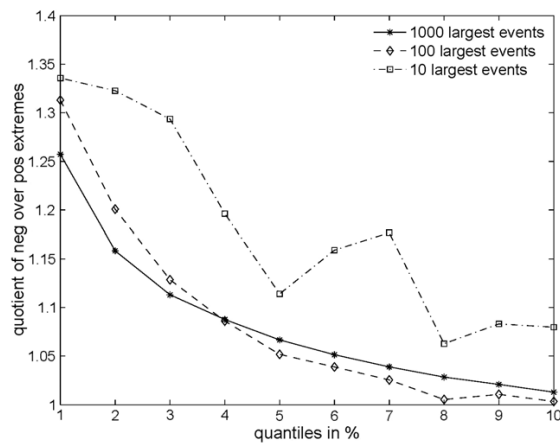


**Figure A.5.** Asymmetry between positive and negative extremes dependent on the number of extremes used for computing the total impact. Shown is the quotient of accumulated carbon of the  $n$  largest negative events over the  $n$  largest positive events for different percentiles (1%, ..., 10%,  $n = 10$  (squares), 100 (diamonds), and 1000 (stars)) averaged over the four data sets MTE, MOD17+, LPJmL, and OCN.

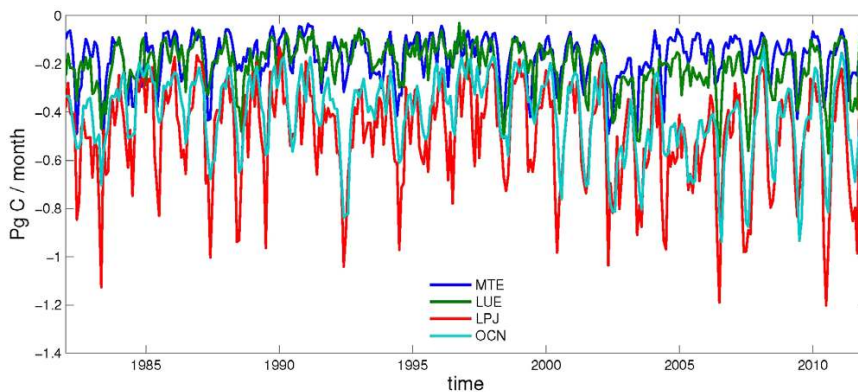


**Figure A.6.** Time series of the 1000 largest tenth-percentile GPP extreme events of the four data sets MTE (blue), LUE (green), LPJ (red), and OCN (cyan). 3D GPP extreme events are transformed into time series as described in section 2.3.

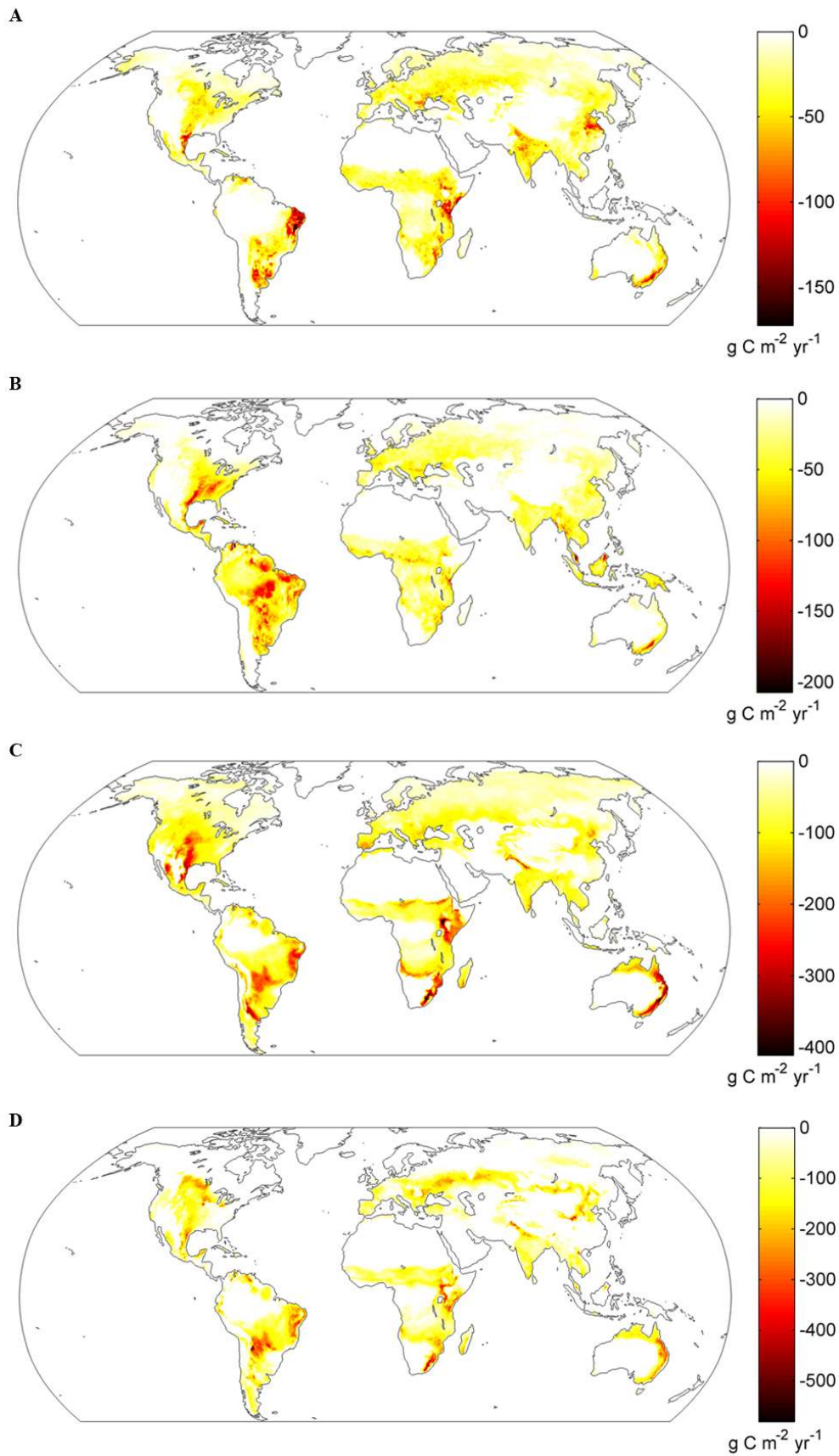


**Figure A.7.** Global distribution of decrease in GPP due to extremes for the four GPP data sets MTE (A), MOD17+ (B), LPJmL (C), and OCN (D). Each pixel depicts the yearly averaged GPP anomalies for the 1000 largest extremes in GPP using the tenth-percentile definition over the whole time period from January 1982 to December 2011. Units are  $\text{g C m}^{-2} \text{ year}^{-1}$ .

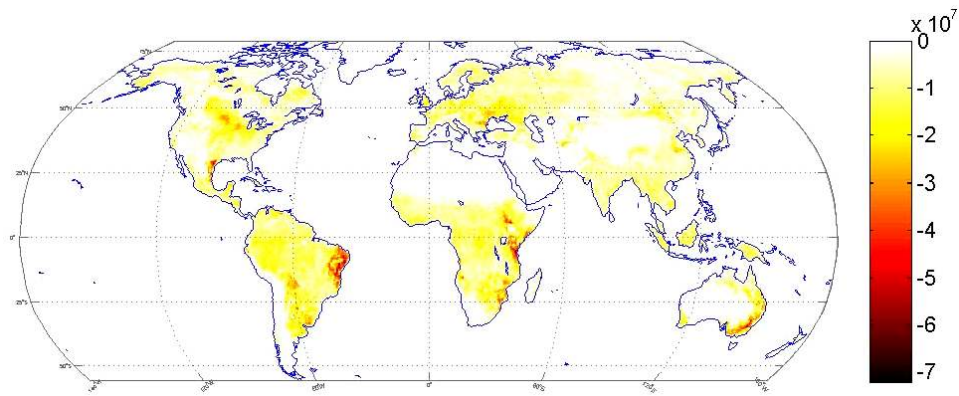


**Figure A.8.** Extremes in the Enhanced Vegetation Index (EVI). Shown are the 1000 largest negative tenth-percentile extremes in EVI. Since EVI is an index between 0 and 1, the units do not have a direct interpretation in gross land carbon uptake. Extremes were computed using the same approach as for GPP.

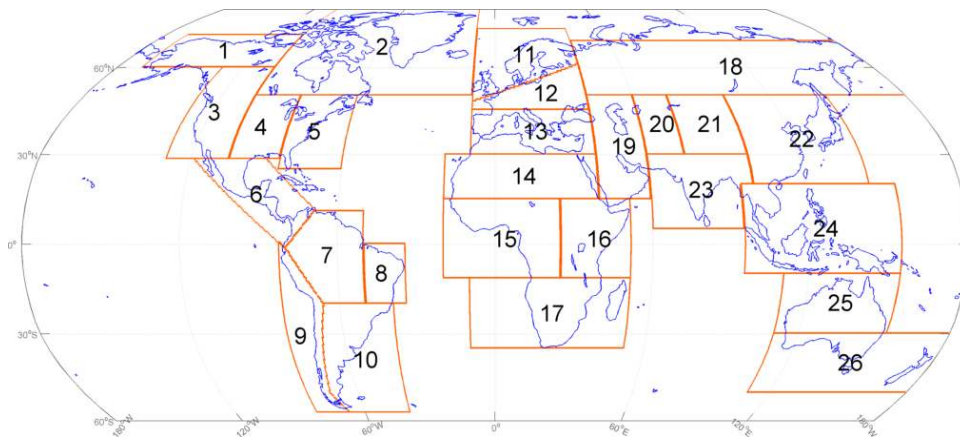


**Figure A.9.** The 26 IPCC regions used in (IPCC).

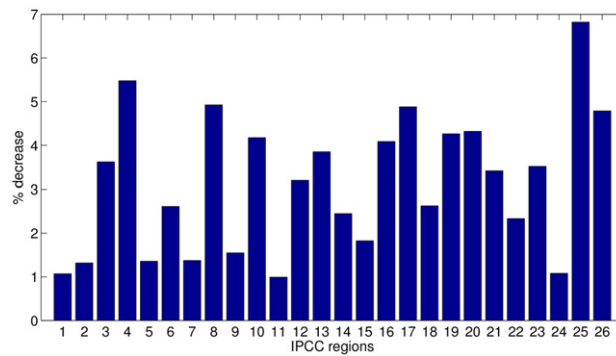


**Figure A.10.** Impact of GPP extremes in the 26 IPCC regions (figure A.9). Decrease in percent of total averaged GPP in each region due to the 1000 largest negative extremes in GPP using the tenth-percentile definition.

References

Aber J D and Federer C A 1992 A generalized, lumped-parameter model of photosynthesis, evapotranspiration and net primary production in temperate and boreal forest ecosystems *Oecologia* **92** 463–74

Baldocchi D et al 2001 FLUXNET: a new tool to study the temporal and spatial variability of ecosystem-scale carbon dioxide, water vapor, and energy flux densities *Bull. Am. Meteorol. Soc.* **82** 2415–34

Barriopedro D, Fischer E M, Luterbacher J, Trigo R M and García-Herrera R 2011 The hot summer of 2010: redrawing the temperature record map of Europe *Science* **332** 220–4

Beer C et al 2010 Terrestrial gross carbon dioxide uptake: global distribution and covariation with climate *Science* **329** 834–8

Bengtsson J, Angelstam P, Elmqvist T, Emanuelsson U, Folke C, Ihse M, Moberg F and Nyström M 2003 Reserves, resilience and dynamic landscapes *Ambio* **32** 389–96

Chen Y, Randerson J T, Morton D C, Defries R S, Collatz G J, Kasibhatla P S, Giglio L, Jin Y and Marlier M E 2011 Forecasting fire season severity in South America using sea surface temperature anomalies *Science* **334** 787–91

Ciais P et al 2005 Europe-wide reduction in primary productivity caused by the heat and drought in 2003 *Nature* **437** 529–33

Clauset A, Shalizi C and Newman M 2009 Power-law distributions in empirical data *SIAM Rev.* **51** 661–703

Dee D P et al 2011 The ERA-Interim reanalysis: configuration and performance of the data assimilation system *Q. J. R. Meteorol. Soc.* **137** 553–97

Dore S, Kolb T E, Montes-Helu M, Sullivan B W, Winslow W D, Hart S C, Kaye J P, Koch G W and Hungate B A 2008 Long-term impact of a stand-replacing fire on ecosystem CO<sub>2</sub> exchange of a ponderosa pine forest *Global Change Biol.* **14** 1801–20

FAO/IIASA/ISRIC/ISSCAS/JRC 2012. Harmonized World Soil Database. FAO, Rome, Italy and IIASA, Laxenburg, Austria

Federer C A 1982 Transpirational supply and demand—plant, soil, and atmospheric effects evaluated by simulation *Water Resour. Res.* **18** 355–62

Fisher J I, Hurtt G C, Thomas R Q and Chambers J Q 2008 Clustered disturbances lead to bias in large-scale estimates based on forest sample plots *Ecol. Lett.* **11** 554–63

Ghil M et al 2011 Extreme events: dynamics, statistics and prediction *Nonlinear Process. Geophys.* **18** 295–350

Giglio L, Randerson J T, van der Werf G R, Kasibhatla P S, Collatz G J, Morton D C and Defries R S 2010 Assessing variability and long-term trends in burned area by merging multiple satellite fire products *Biogeosciences* **7** 1171–86

Huete A, Didan K, Miura T, Rodriguez E P, Gao X and Ferreira L G 2002 Overview of the radiometric and biophysical performance of the MODIS vegetation indices *Remote Sens. Environ.* **83** 195–213

Huntington T G 2006 Evidence for intensification of the global water cycle: Review and synthesis *J. Hydrol.* **319** 83–95

IPCC 2012. *Managing the Risks of Extreme Events and Disasters to Advance Climate Change Adaptation* (Cambridge: Cambridge University Press)

Jung M et al 2011 Global patterns of land-atmosphere fluxes of carbon dioxide, latent heat, and sensible heat derived from eddy covariance, satellite, and meteorological observations *J. Geophys. Res.* **116** G00J07

Keenan T F et al 2012 Terrestrial biosphere model performance for inter-annual variability of land-atmosphere CO<sub>2</sub> exchange *Global Change Biol.* **18** 1971–87

Kleidon A and Heimann M 1998 A method of determining rooting depth from a terrestrial biosphere model and its impacts on the global water and carbon cycle *Global Change Biol.* **4** 275–86

Körner C 2003 Atmospheric science. Slow in, rapid out—carbon flux studies and Kyoto targets *Science* **300** 1242–3

Krinner G, Viovy N, de Noblet-Ducoudre N, Ogee J, Polcher J, Friedlingstein P, Ciais P, Sitch S and Prentice I C 2005 A dynamic global vegetation model for studies of the coupled atmosphere–biosphere system *Global Biogeochem. Cycles* **19** GB1015

Le Quéré C, Andres R, Boden T, Conway T, Houghton R, House J, Marland G, Peters G, van der Werf G and Ahlström A 2013 The global carbon budget 1959–2011 *Earth Syst. Sci. Data* **5** 165–85

Lewis S L, Brando P M, Phillips O L, van der Heijden G M F and Nepstad D 2011 The 2010 Amazon drought *Science* **331** 554

Lloyd-Hughes B 2012 A spatio-temporal structure-based approach to drought characterisation *Int. J. Climatol.* **32** 406–18

Ma Z, Peng C, Zhu Q, Chen H, Yu G, Li W, Zhou X, Wang W and Zhang W 2012 Regional drought-induced reduction in the biomass carbon sink of Canada’s boreal forests *Proc. Natl Acad. Sci. USA* **109** 2423–7

Mahecha M, Reichstein M and Carvalhais N 2010 Global convergence in the temperature sensitivity of respiration at ecosystem level *Science* **329** 838–40

Mueller B and Seneviratne S I 2012 Hot days induced by precipitation deficits at the global scale *Proc. Natl Acad. Sci.* **109** 12398–403

Peters W et al 2007 An atmospheric perspective on North American carbon dioxide exchange: CarbonTracker *Proc. Natl Acad. Sci. USA* **104** 18925–30

Piao S et al 2010 The impacts of climate change on water resources and agriculture in China *Nature* **467** 43–51

Potter C, Tan P-N, Steinbach M, Klooster S, Kumar V, Myneni R and Genovesi V 2003 Major disturbance events in terrestrial ecosystems detected using global satellite data sets *Global Change Biol.* **9** 1005–21

Prentice I C, Bartlein P J and Webb T 1993 Vegetation and climate-change in Eastern North-America since the last glacial maximum (Vol 72, Pg 2038, 1993) *Ecology* **74** 998

Reichstein M et al 2013 Climate extremes and the carbon cycle *Nature* **500** 287–95

Reichstein M et al 2007 Reduction of ecosystem productivity and respiration during the European summer 2003 climate anomaly: a joint flux tower, remote sensing and modelling analysis *Global Change Biol.* **13** 634–51

Richardson A D, Hollinger D Y, Aber J D, Ollinger S V and Braswell B H 2007 Environmental variation is directly responsible for short- but not long-term variation in forest-atmosphere carbon exchange *Global Change Biol.* **13** 788–803

Rosenzweig C, Iglesias A and Yang X 2001 Climate change and extreme weather events; implications for food production, plant diseases, and pests *Global Change Hum. Health* **2** 90–104

Running S W, Nemani R R, Heinsch F A, Zhao M S, Reeves M and Hashimoto H 2004 A continuous satellite-derived measure of global terrestrial primary production *Bioscience* **54** 547–60

Running S W, Thornton P E, Nemani R and Glassy J M 2000 *Global Terrestrial Gross and Net Primary Productivity from the Earth Observing System* in *Methods in Ecosystem Science* (New York: Springer) pp 44–57

Seneviratne S I et al 2012 Changes in climate extremes and their impacts on the natural physical environment *A Special Report of Working Groups I and II of the Intergovernmental Panel on Climate Change* ed C B Field et al (Cambridge: Cambridge University Press) pp 109–230

Sillmann J, Kharin V V, Zwiers F W, Zhang X and Bronaugh D 2013 Climate extremes indices in the CMIP5 multimodel

- ensemble: part 2. Future climate projections *J. Geophys. Res.-Atmos.* **118** 2473–93
- Sitch S *et al* 2003 Evaluation of ecosystem dynamics, plant geography and terrestrial carbon cycling in the LPJ dynamic global vegetation model *Global Change Biol.* **9** 161–85
- Smith M D 2011 An ecological perspective on extreme climatic events: a synthetic definition and framework to guide future research *J. Ecol.* **99** 656–63
- Teuling A J, Seneviratne S I, Williams C and Troch P A 2006 Observed timescales of evapotranspiration response to soil moisture *Geophys. Res. Lett.* **33** L23403
- Zaehle S and Friend A D 2010 Carbon and nitrogen cycle dynamics in the O–CN land surface model: 1. Model description, site-scale evaluation, and sensitivity to parameter estimates *Global Biogeochem. Cycles* **24** GB1005
- Zaehle S, Friend A D, Friedlingstein P, Dentener F, Peylin P and Schulz M 2010 Carbon and nitrogen cycle dynamics in the O–CN land surface model: 2. Role of the nitrogen cycle in the historical terrestrial carbon balance *Global Biogeochem. Cycles* **24** GB1006
- Zhao M and Running S W 2010 Drought-induced reduction in global terrestrial net primary production from 2000 through 2009 *Science* **329** 940–3
- Zscheischler J, Mahecha M D, Harmeling S and Reichstein M 2013 Detection and attribution of large spatiotemporal extreme events in Earth observation data *Ecol. Inform.* **15** 66–73